

Monolithic On-Chip Phononic Chiral Anomalous Bulk States on LiNbO₃ Thin-films

Zhe Li¹, Zhen-Hui Qin¹, Shu-Mao Wu¹, Chen-Bei Hao¹, Fan-Yun Pan¹, Hao Yan¹, Yi-Han He¹, Yan-Shen Zhou¹, Xue-Jun Yan^{1,2,3}, Si-Yuan Yu^{1,2,3*}, Cheng He^{1,2,3}, Ming-Hui Lu^{1,2,3}, and Yan-Feng Chen^{1,2,3*}

¹National Laboratory of Solid-State Microstructures & Department of Materials Science and Engineering, Nanjing University, Nanjing 210093, China.

²Collaborative Innovation Center of Advanced Microstructures, Nanjing University, Nanjing 210093, China

³Jiangsu Key Laboratory of Artificial Functional Materials, Nanjing University, Nanjing, 210093, China

*corresponding author. e-mail: yusiyuan@nju.edu.cn; yfchen@nju.edu.cn

Phononic materials are crucial for developing efficient, robust mechanical waveguides with strong transport properties, enabling advances in sensing, signal processing, energy harvesting, and microfluidics. A key motivation is their integration into monolithic systems for on-chip applications. While topological phononic materials developed in the past decade offer unidirectional edge states immune to backscattering, their integration requires large volumes to control localized small volumes' transport properties, limiting their efficiency and application in modern phononic circuits. The recently introduced chiral anomalous bulk states (CABSs) combine the advantages of topological materials with innovative boundary designs, overcoming transmission limitations and ensuring full material utilization for superior wave propagation. Here, we present the first on-chip monolithic CABS device integrated on a suspended LiNbO₃ thin film. This breakthrough enables the creation of phononic waveguides with unmatched unidirectionality, low loss, and high transmission efficiency, seamlessly integrated with broadband piezoelectric transducers, and showcasing their potential for high-fidelity, broad-bandwidth microwave signal transmission. Additionally, we exploit the slow-wave characteristics of CABSs for delay lines and high-density signal processing. Tailoring wave propagation through boundary engineering opens a new paradigm for phononic/photonic device design, with implications across microelectronics, high-frequency communications, radar, and advanced sensing technologies. The work sets the stage for the future development of highly scalable, multifunctional, and robust phononic systems, unlocking new avenues for integrated acoustic technologies.

Efficient mechanical waveguides hold profound significance in both scientific research and engineering applications. Topologically protected states have attracted considerable attention due to their resistance to backscattering [1-5], which enables the creation of waveguides immune to defects, while also facilitating low-loss transmission over large angles and extended distances. Traditional methods for constructing such waveguides often rely on two topologically distinct phononic crystals to create boundary states [6-15]. However, these approaches face significant challenges when integrated into large-scale phononic devices on chips [12-19]. For example, the broadband piezoelectric transducers used in on-chip phononic devices—such as surface acoustic wave and Lamb wave devices [20-23]—feature large apertures, far exceeding the small apertures of topological boundary waveguides. This mismatch leads to a minimal proportion of the on-chip acoustic waves being coupled into the topological waveguide, resulting in challenges such as low signal-to-noise ratio, high loss, and crosstalk [14-16,18,19]. Recently, the concept of boundary-induced chiral anomalous bulk states (BI-CABSs) has emerged [24-28], facilitating the simultaneous realization of previously conflicting advantages—unidirectionality, wide bandwidth, large apertures, and high material efficiency—within a single waveguide. This breakthrough opens up exciting new avenues for the development of phononic integrated devices that exhibit backscattering immunity. While traditional topological approaches manipulate the bulk material to control boundary transmission characteristics, BI-CABSs adopt an alternative strategy, designing the material's boundary to induce bulk states with exceptional transmission properties. BI-CABSs have been demonstrated in both airborne [24] and solid-state acoustic waves [25-27], but fully integrated on-chip BI-CABS phononic devices have yet to be realized.

In this work, we present the first realization of an on-chip, monolithic BI-CABS phononic crystal integrated device. Specifically, we fabricate a circular hole array with a honeycomb lattice on a 300 nm-thick suspended single-crystal lithium niobate (LiNbO_3) film, successfully realizing a quadruple-degenerate Dirac point at the reciprocal space center of the two-dimensional A-mode Lamb wave phononic crystal—marking the emergence of a two-dimensional phononic semi-metal with pseudospin characteristics. By meticulously tuning the spatial configuration of the free boundary conditions along one dimension, we achieve the propagation of phononic BI-CABSs along the orthogonal dimension. Laser vibrometry experiments confirm the existence of these BI-CABSs across a range of apertures, operating at very high frequencies (VHF). Moreover, we demonstrate a "microwave-acoustic-microwave" transmission line with 100% material efficiency, perfectly matched to an advanced on-chip piezoelectric transducer. This material-integrated system not only highlights the advantages of BI-CABSs—such as backscattering resistance, low loss, wide bandwidth, small dispersion, and ultra-low sound velocity—but also underscores its potential applications in signal unidirectional transmission and delay processing.

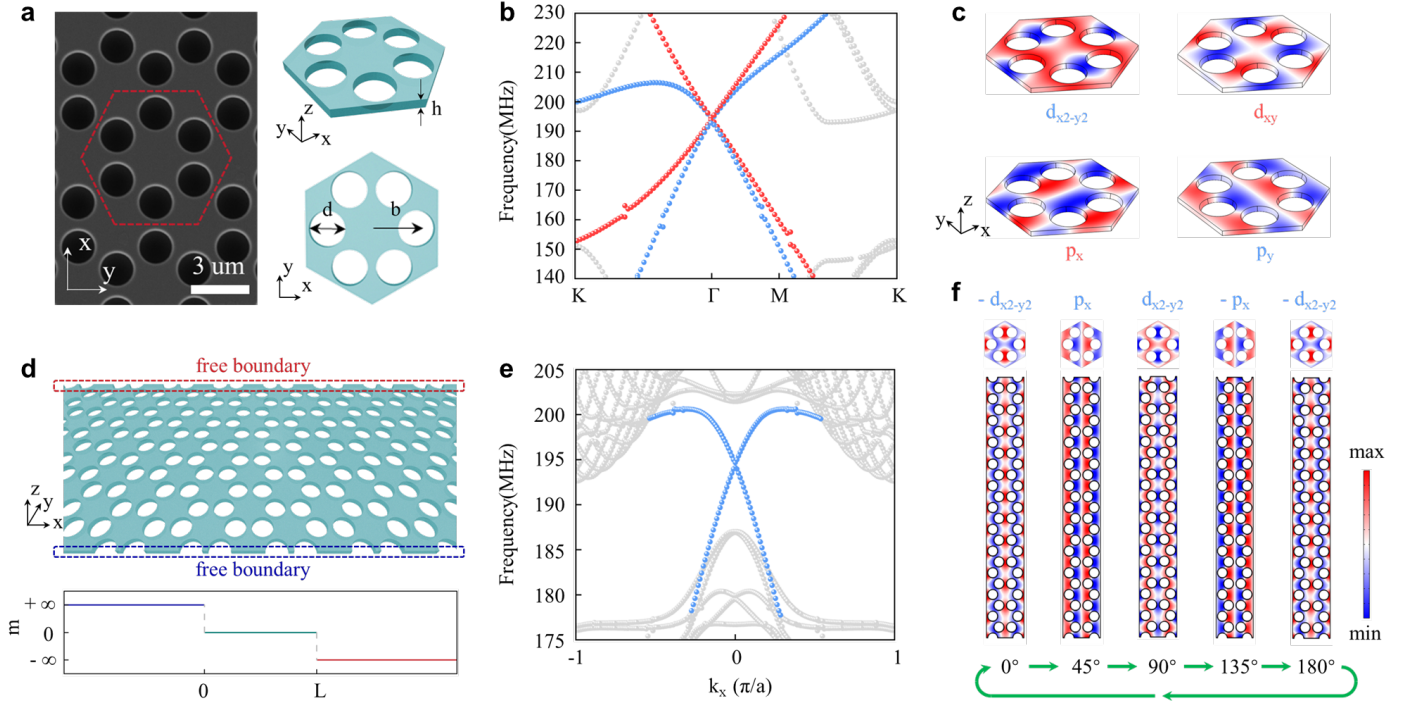


Figure 1. Phononic quadruple degeneracy and the emergence of BI-CABSs. (a) Scanning electron microscope image (inset) and schematic diagram of the phononic crystal with a honeycomb lattice structure. (b) Band structure of the phononic crystal, featuring the quadruple degeneracy at the center of the Brillouin zone. (c) Out-of-plane displacement patterns of the four degenerate Lamb wave modes at the center of the Brillouin zone, analogous to electronic p/d orbitals. (d) Schematic of the phononic crystal with a pair of free boundaries along the x -direction, and the resulting Dirac mass function due to the boundary-induced chiral anomaly. (e) Projected band structure of the BI-CABSs, illustrating the emergence of Dirac-like dispersion due to boundary-induced anomalies. (f) Out-of-plane displacement of the BI-CABSs at different phases, showing the pseudospin characteristics of the bulk modes, corresponding to the p_x and $d_{x^2-y^2}$ symmetry.

Phononic BI-CABSs based on suspended LiNbO_3 thin films.

We designed a Lamb wave phononic crystal with a honeycomb lattice structure (see Fig. 1a). The unit cell consists of six circular holes, each with a diameter of $1.97 \mu\text{m}$, a lattice constant of $7.14 \mu\text{m}$, and a distance of $2.38 \mu\text{m}$ between the center of the circular holes and the center of the unit cell. These holes were etched into a 300 nm -thick Y128-cut LiNbO_3 film using an ICP-RIE process. A subsequent wet etching process with buffered oxide etch (BOE) solution was applied to remove the silicon dioxide sacrificial layer beneath the LiNbO_3 film, thus suspending the phononic crystal membrane. This phononic crystal exhibits C_{6v} point group symmetry. When considering only out-of-plane deformation, it displays a quadruple degeneracy at the center of the Brillouin zone (see Fig. 1b, and more in Supplementary Information Note 1). These degenerate modes

correspond to the high-frequency $d_{x^2-y^2}/d_{xy}$ bulk modes and the low-frequency p_x/p_y bulk modes[7, 9]. These modes resemble the p and d orbitals in electron systems. Specifically, the $d_{x^2-y^2}$ mode exhibits a symmetry of $\delta_x/\delta_y = 1/1$, the d_{xy} mode follows the $-1/-1$ symmetry, the p_x mode exhibits a $-1/1$ symmetry, and the p_y mode exhibits a $1/-1$ symmetry. Here, $\delta_x/\delta_y = 1/-1$ denotes even or odd symmetry along the x or y axis. These modes can be viewed as simulating a two-dimensional phononic semi-metal with pseudospin characteristics.

To reduce the periodicity of this two-dimensional phononic semi-metal, we introduce a pair of free boundaries along the y -direction, positioned at the mirror symmetry planes of the outermost unit cells (see Fig. 1d). The introduction of these free boundaries breaks the chiral conservation within the phononic crystal (see Fig. 1e). Specifically, two weakly dispersive bands crossing at the center of the Brillouin zone, which should correspond to the odd and even modes in the absence of boundaries, are now both associated with the even mode. This is because the free boundary conditions prevent the out-of-plane deformation from remaining zero at the boundaries. The odd modes (p_y/d_{xy}), due to the deformation being zero at the mirror symmetry plane, cannot satisfy the boundary condition. Therefore, only even modes ($p_x/d_{x^2-y^2}$) remain in the phononic crystal, with their deformation not remaining zero at the mirror symmetry plane—this is the origin of the boundary-induced chiral anomalous states. These chiral anomalous states are bulk transmission modes, with their wavevectors spanning the entire Brillouin zone, and their energy is uniformly distributed across the phononic crystal (see Fig. 1f).

The theoretical explanation for the emergence of these BI-CABS is as follows. Consider a phononic crystal under boundary constraints with a width of L , with free boundaries positioned at $y = 0$ and $y = L$. The Dirac Hamiltonian of this phononic crystal can be expressed as: $H(y) = \delta_x k_x v_D - i \partial_y \delta_y v_D + m(y) \delta_z$. The boundary conditions result in a step-like mass function at the Dirac point[23] (see Fig. 1d): $m(y) = m_1$ for $y < 0$; $m(y) = 0$ for $0 \leq y \leq L$; $m(y) = m_2$ for $y > L$. The Hamiltonian in the region $0 \leq y \leq L$ exhibits mirror symmetry along the y -direction, satisfying $\delta_x H(y) \delta_x = H(-y)$. Therefore, the eigenfunctions at the Dirac point can be expressed as:

$$\psi = \begin{cases} e^{|m_1|y} \begin{pmatrix} 1 \\ \text{sgn}(m_1) \end{pmatrix} & y \leq 0 \\ \begin{pmatrix} 1 \\ \pm 1 \end{pmatrix} & 0 \leq y \leq L \\ e^{-|m_2|(y-L)} \begin{pmatrix} 1 \\ -\text{sgn}(m_2) \end{pmatrix} & y \geq L \end{cases} \quad (1)$$

Due to the boundary continuity, the wavefunction can only have two possible solutions. When $m_1 > 0$ and $m_2 < 0$, an even mode solution $\psi = (1 | 1)$ exists; when $m_1 < 0$ and $m_2 > 0$, an odd mode solution $\psi = (1 | -1)$ exists. This indicates that only one mode exists in the phononic crystal, and the type of mode is determined by the sign of the Dirac mass at the edges of the phononic crystal. Furthermore, the step-like nature of the mass function causes the wavefunction to exponentially decay outside the phononic crystal. When $|m_1| = |m_2|$

$= m_0 \rightarrow +\infty$, the acoustic waves cannot penetrate the boundaries of the phononic crystal, and the wavefunction becomes localized within the interior region of the crystal, thus forming a bulk mode. BI-CABSs can also be described by a tight binding model, see Supplementary Information Note 2.

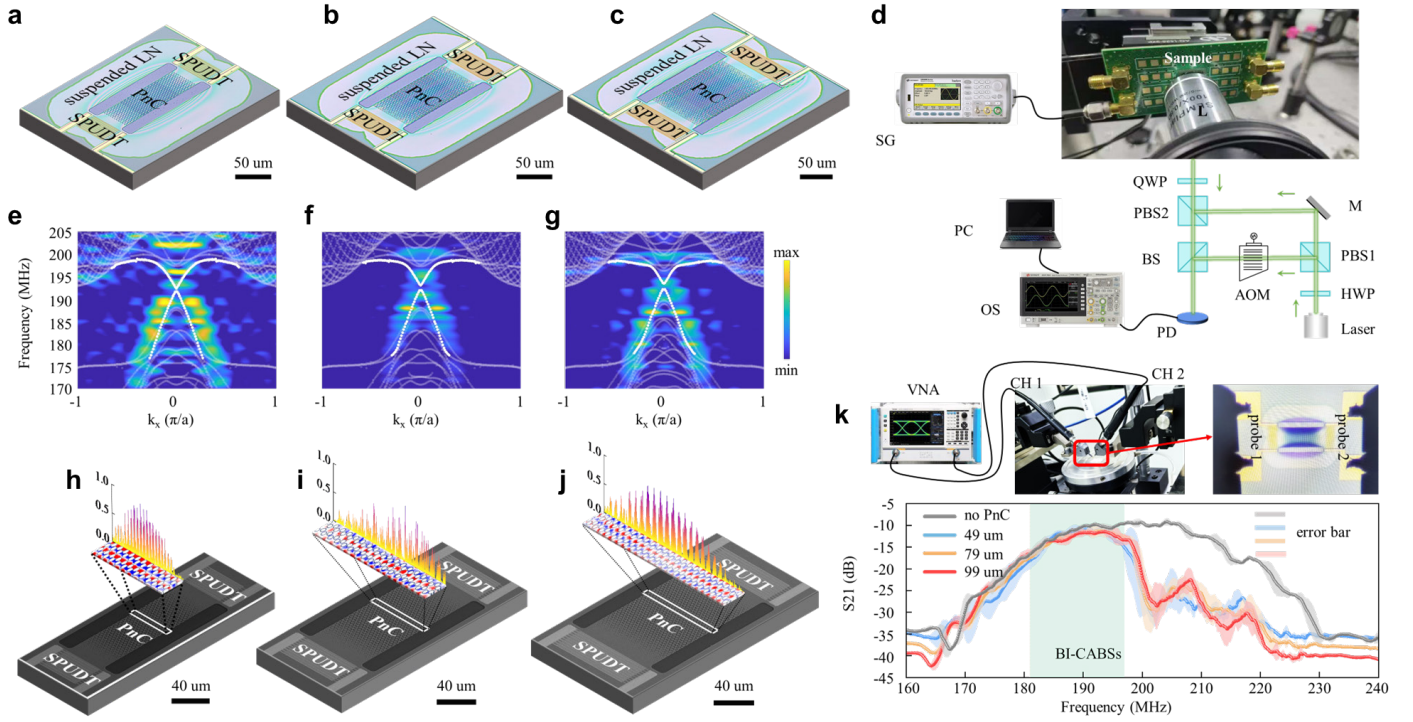


Figure 2. “Microwave-acoustic-microwave” signal transmission lines with BI-CABSs. (a)-(c) Optical images of three transmission lines with aperture sizes of 49 μm , 79 μm , and 99 μm , respectively. (d) Schematic diagram of the laser vibrometer used in the experiments (see Methods for the optical path principle). (e)-(g) Calculated and experimentally obtained projected band structures of BI-CABSs (h)-(j) (bottom) SEM images of the transmission lines. (middle) Experimentally measured out-of-plane displacement field. (top) Experimentally measured out-of-plane amplitude distributions across the phononic crystal regions. (k) Measured transmission coefficient (S_{21}) as a function of excitation frequency for transmission lines with and without the phononic crystal, comparing the BI-CABSs transmission lines with different aperture sizes.

On-chip monolithic Lamb wave phononic BI-CABSs integrated transmission lines.

As discussed earlier, a key advantage of BI-CABSs is their ability to fully utilize the material, with the waveguide aperture perfectly matching that of the broadband transducers. We successfully fabricated “microwave-acoustic-microwave” signal transmission lines with three different aperture sizes (Fig. 2a-2c) by depositing single-phase unidirectional transducers (SPUDTs) at both ends of the phononic crystal using electron beam evaporation (EBE) and lift-off techniques. These transmission lines exhibited perfect matching between the anti-reflection bulk states and the advanced on-chip microwave transducers. The SPUDTs used

in our experiment were designed to excite the unidirectional A0-mode Lamb waves.[29] The transducers consisted of three distinct electrodes: a reflective electrode, a grounding electrode, and a signal electrode. The reflective electrode weakened the acoustic waves in one direction and enhanced them in the opposite direction, ensuring unidirectional excitation. To maximize the electromechanical coupling efficiency of the A0-mode Lamb waves, we selected the Y128-cut configuration for the LiNbO₃ film.

To verify that the transducers could excite the BI-CABSs within the phononic crystal, we used a laser vibrometer (Fig. 2d) to scan the out-of-plane (Z-direction) displacement field of the phononic crystal at different frequencies, constructing the band structure along the X-direction (Fig. 2e-2g). As shown, the three phononic crystals with different aperture sizes exhibited characteristic band features of the BI-CABSs, with experimental results closely matching the simulation results (solid white lines). At a specific frequency of 187 MHz, the experimentally measured out-of-plane displacement field (Fig. 2h-2j) demonstrated the bulk mode distribution across the entire phononic crystal, confirming that the transmission mode in this case was a bulk state.

One of the most significant advantages of BI-CABSs is their ability to achieve low-loss signal transmission. The S_{21} parameters of the three dual-port transmission lines containing BI-CABSs verified this (Fig. 2k). Through microwave signal transmission experiments with dual-port measurements, we confirmed that the BI-CABS transmission lines operated with nearly perfect transmission, with the S_{21} parameter remaining constant. Specifically, the conventional transmission lines without the phononic crystal exhibited high signal transmission over a frequency range of 180-210 MHz. In contrast, the transmission lines incorporating the BICAs phononic crystal showed a narrower bandwidth of 180-195 MHz, corresponding to the frequency range of the BI-CABSs, with no significant drop in the S_{21} parameter within this band. On the other hand, at frequencies within the phononic crystal's bandgap (*e.g.*, above 195 MHz), the acoustic waves excited by the transducer experienced attenuation within the phononic crystal, causing a decrease in the S_{21} parameter by 10-15 dB.

Verification of backscattering resistance of on-chip phononic BI-CABSs.

To further verify the backscattering resistance of BI-CABSs, we conducted a series of control experiments by introducing defects into both BI-CABSs phononic crystal transmission lines and transmission lines without phononic crystals (see Figs. 3a, 3b). The energy field distribution and out-of-plane displacement field distribution of the entire device, obtained through finite element simulations (Figs. 3c, 3d), demonstrate the backscattering resistance of BI-CABSs. In the BI-CABSs transmission line, Lamb waves efficiently propagate through multiple randomly distributed defects along the width direction. Despite the presence of these defects, the energy transmission remains high, and the phase of the transmitted wave remains stable, preserving the

plane wave nature. In contrast, after introducing defects of similar size and quantity in the transmission line without a phononic crystal, there is a significant reduction in transmitted energy, and the phase of the transmitted wave becomes severely disordered, losing its plane wave characteristics.

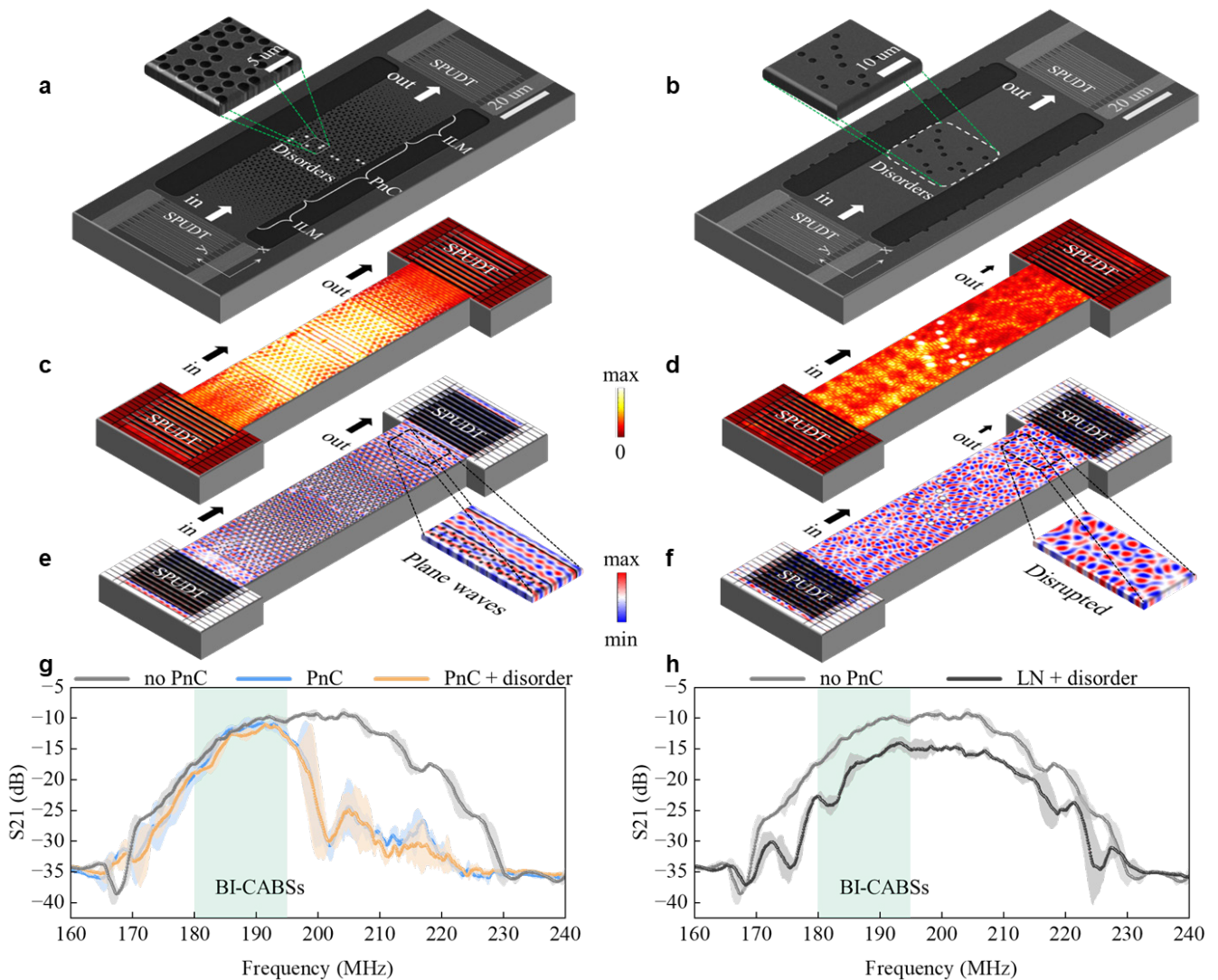


Figure 3. Verification of backscattering resistance in phononic BI-CABSs. (Left panels)

Transmission line with BI-CABS phononic crystals; (Right panels) Transmission line without

phononic crystals. (a)-(b) SEM images of the two transmission lines, each with embedded

defects. (c)-(d) Simulated energy field distributions for the transmission lines with and without

phononic crystals, highlighting the backscattering resistance in the BI-CABS line. (e)-(f)

Simulated out-of-plane displacement fields for the two devices. In (e), the plane wave maintains

its form after passing through defects, indicating backscattering suppression in the BI-CABS line.

In (f), the plane wave is distorted, highlighting the absence of backscattering resistance.

(g)-(h) Measured transmission coefficient (S_{21}) as a function of excitation frequency for both devices,

demonstrating the superior performance of the BI-CABSs transmission line under the presence

of defects.

Experimentally, we further validated the backscattering resistance of BI-CABSs through S_{21} measurements of the dual-port transmission lines (Fig. 3g). The S_{21} parameter of the BI-CABSs transmission line showed almost no change after the introduction of defects, particularly within the working frequency range of BICAs (approximately 180-195 MHz), where the performance remained notably stable. In contrast (Fig. 3h), the S_{21} parameter of the transmission line without phononic crystals showed a significant decrease across the entire frequency range of the transducer (approximately 170-230 MHz) after the introduction of defects.

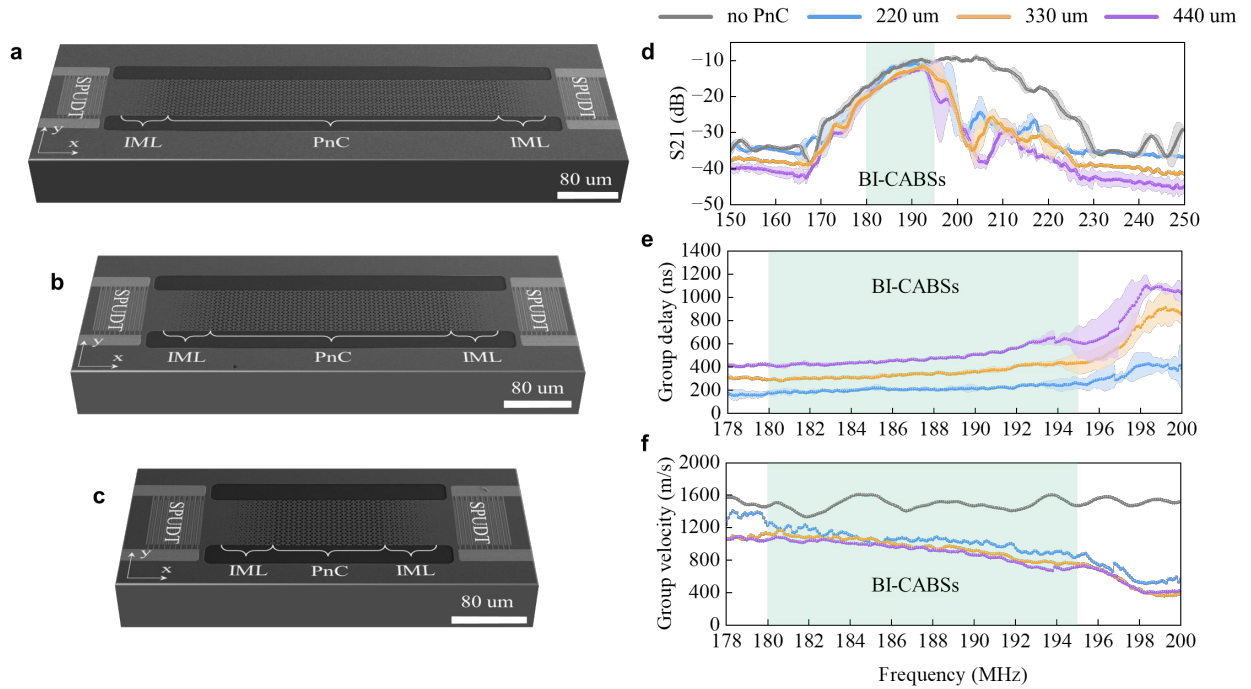


Figure 4. Slow-wave delay lines based on phononic BI-CABSs. (a)-(c) Schematic diagrams of the three delay lines incorporating BI-CABSs phononic crystals, each with an aperture size of $49 \mu\text{m}$ and lengths of $220 \mu\text{m}$, $330 \mu\text{m}$, and $440 \mu\text{m}$, respectively. (d) S_{21} parameter measurements for the delay lines, showing consistent transmission characteristics within the BI-CABSs working frequency range. (e) Group delay measurements for the delay lines of different lengths, demonstrating a linear increase in group delay with device length, reaching a maximum of approximately 600 ns . (f) Group velocity measurements for the delay lines, illustrating the weak dispersion characteristics of BI-CABSs, with Lamb wave velocity decreasing as frequency increases, reaching as low as $\sim 600 \text{ m/s}$.

Slow-wave delay line based on phononic BI-CABSs.

In addition to its broadband capability and backscattering resistance, the BI-CABSs we developed also exhibit slow-wave characteristics. Slow-wave devices are of significant importance for applications that require higher information and energy density, as well as enhanced interaction between waves and matter. In integrated

phononic devices, key applications of slow waves include signal delayers, convolvers, and sensors. In our experiment, we designed delay lines incorporating BI-CABSs phononic crystals with three different lengths (Fig. 4a-4c). All delay lines have the same aperture size (49 μm), but their lengths, defined as the distance between the centers of the two pairs of transducers, are 220 μm , 330 μm , and 440 μm , respectively. The ratio of the length to the film thickness in the BI-CABSs phononic crystals made from lithium niobate films is as high as an astonishing 1400 times, an exceptionally large span in both microstructure and even macroarchitecture, which is rare in current reports.

A significant advantage brought by our BI-CABSs for delay lines is the ability to achieve long-distance, low-speed, and low-loss robust transmission of phonon signals. The two-port transmission experiments show that the S_{21} parameters of the three delay lines with different lengths remain nearly the same—within the BI-CABSs working frequency range, their S_{21} values are almost identical to those of transmission lines without a phononic crystal (Fig. 4d). We further tested the group delay of the three delay lines (Fig. 4e). The results show that the group delay increases linearly with the length of the device, reaching a maximum of about 400 ns. Additionally, the group delay of the three devices is monotonic and continuous within the BI-CABSs working frequency range. In the relatively low-frequency range, the delay remains stable with only slight increases; in the higher frequency range, the delay gradually increases with frequency, which is consistent with the relatively weak dispersion of the BI-CABSs and meets the practical engineering requirements.

Based on the experimental measurements of the group delay, we calculated the group velocity of the BI-CABSs (Fig. 4f), which further confirms its weak dispersion characteristics. The group velocity decreases with increasing frequency, and throughout the working frequency range, the velocity remains below approximately 1100 m/s, with the lowest dropping to about 600 m/s. The variation in velocity with frequency is consistent with the slope of the BI-CABSs band structure and is independent of the device length. Compared to transmission lines without phononic crystals, the group velocity in the BI-CABSs phononic crystal is significantly reduced. For example, at 187 MHz, the velocity in the conventional transmission line is about 1600 m/s, while in the BI-CABSs transmission line, it drops to approximately 900 m/s.

Conclusion & Discussion

This study introduces the integration of BI-CABSs into on-chip phononic devices, marking a significant advancement in phononic materials with broadband, backscattering-resistant, and slow-wave properties. One of the key advantages of BI-CABSs is their ability to fully utilize materials and provide sufficiently large transmission apertures, ensuring efficient signal transmission and scalability. This capability makes BI-CABSs ideal for high-performance devices in signal processing, sensing, and phononic computing. The successful integration of BI-CABSs into scalable, monolithic devices compatible with microelectronic platforms

highlights their potential for large-scale adoption in advanced phononic systems.

BI-CABSs are not limited to the material used in this study (LiNbO_3); their versatility extends to other piezoelectric single crystals such as LiTaO_3 , AlN , and GaN , as well as widely used silicon-based materials like Si , SiO_2 , SiN , and SiC . Additionally, the integration of piezoelectric 2D materials further enhances device miniaturization and performance. This material flexibility enables optimized devices for diverse applications, from microelectronics to photonics and sensing, offering substantial potential for integrated phononic technologies. Moreover, the frequency range of BI-CABSs can be extended through advances in MEMS/NEMS fabrication techniques, facilitating operation at GHz frequencies and beyond for applications in high-frequency communications, radar, and data transmission.

The BI-CABSs demonstrated here show a bandwidth of approximately 7%, which could be further enhanced through topological optimization or inverse design techniques, enabling broader bandwidths in future devices. While the current devices show some linear dispersion, this can be minimized through optimization, potentially achieving fully dispersion-free operation. These improvements will enhance the efficiency of phononic devices, paving the way for the next generation of low-loss, highly scalable acoustic technologies. In conclusion, BI-CABSs provide a transformative approach to phononic device design, offering tunable wave propagation characteristics that can be customized across various materials, frequencies, and applications. This work lays the foundation for future innovations in integrated phononics, with broad implications for materials science, condensed matter physics, and acoustic technologies, heralding the emergence of multifunctional, robust, and scalable phononic systems.

Methods

Device Fabrication

The devices were fabricated on a four-layer substrate consisting of a 500 μm -thick silicon (Si) base layer, a 1 μm -thick poly-silicon oxide (P-SiO_2) layer, a 2 μm -thick silicon dioxide (SiO_2) sacrificial layer, and a 300 nm-thick LiNbO_3 layer. The fabrication process involved three main steps (See more in Supplementary Information Note 3):

1. **Phononic Crystal Fabrication:** A chromium (Cr) metal layer was first deposited on the LiNbO_3 surface as a hard mask, followed by the deposition of a silicon (Si) film to enhance etch resistance. ZEP photoresist was spin-coated onto the silicon film, and the phononic crystal pattern was defined using electron beam lithography (EBL). The pattern was then transferred layer by layer by sequential etching of the silicon film, Cr hard mask, and LiNbO_3 using inductively coupled plasma reactive ion etching (ICP-RIE). In order to avoid the reflection caused by the mismatch of acoustic impedance when acoustic waves enter the phononic crystal in LiNbO_3 thin film and exit from the phononic crystal, we designed impedance matching layers (IMLs) at the acoustic wave

incident and exit boundaries of the phononic crystal, see more in Supplementary Information Note 4.

- 2. Single-phase unidirectional transducers (SPUDTs) Preparation:** ZEP photoresist was spin-coated onto the LiNbO₃ surface, and the SPUDTs pattern was defined using EBL. A chromium (Cr) adhesion layer followed by a gold (Au) film were sequentially deposited using electron beam evaporation (EBE). The excess metal was removed via a lift-off process to obtain the desired SPUDTs structure.
- 3. Device Suspension:** The wafer was immersed in buffered oxide etch (BOE) solution to remove the SiO₂ sacrificial layer beneath the LiNbO₃, thereby suspending the device structure. Finally, the suspended structure was released using supercritical drying to avoid stiction or collapse due to surface tension.

Numerical simulations

Full-wave simulations were performed using the commercial finite element software COMSOL Multiphysics. For the band structure calculation, three-dimensional unit cells arranged in a honeycomb lattice were employed, each containing six air holes on a Y128-cut suspended LiNbO₃ thin film. Floquet periodic boundary conditions were applied to these unit cells. In all samples shown in Figs. 1e and 2–4, free boundaries were placed along the y-direction. The material properties used for the LiNbO₃ membrane are as follows: **Elastic constants:** $c_{11} = c_{22} = 202.9$ GPa, $c_{12} = 52.9$ GPa, $c_{13} = c_{23} = 74.9$ GPa, $c_{33} = 243.1$ GPa, $c_{14} = c_{56} = 9$ GPa, $c_{24} = -9$ GPa, $c_{44} = c_{55} = 60$ GPa, $c_{66} = 74.9$ GPa; **Piezoelectric coefficients:** $e_{21} = -2.5$ C/m², $e_{31} = e_{32} = 0.19$ C/m², $e_{22} = 2.5$ C/m², $e_{33} = 1.3$ C/m², $e_{24} = e_{15} = 3.7$ C/m², $e_{16} = -2.5$ C/m²

Measurements

A two-port transmission experiment was conducted using a probe station combined with a vector network analyzer to measure the S21 parameters of the device. To examine the out-of-plane deformation field distribution of the phononic crystal, a laser Doppler vibrometer was used. The optical path is as follows: The laser is split by a polarizing beam splitter (PBS1) into object and reference beams. The object beam is reflected by a mirror (M) and focused onto the sample surface by an objective lens (L). The reflected beam from the sample is directed to a beam splitter (BS) via PBS2. The reference beam is frequency-shifted by an acousto-optic modulator (AOM) and directed to the BS. The reflected beam from the sample and the reference beam combine and interfere at the BS, with the resulting interference pattern detected by a photodetector (PD). A half-wave plate (HWP) adjusts the intensity of the two beams for optimal interference, and a quarter-wave plate (QWP) reduces the intensity of the reflected light returning to the laser, protecting it from damage.

Data availability. The data supporting the plots and findings presented in this study are available from the corresponding authors upon reasonable request.

References

- [1] Hasan, M. Z., & Kane, C. L. (2010). Colloquium: Topological insulators. *Reviews of Modern Physics*, 82(4), 3045–3067.
- [2] Lu, L., Joannopoulos, J. D., & Soljačić, M. (2014). Topological photonics. *Nature Photonics*, 8(11), 821–829.
- [3] Zhang, X., Zangeneh-Nejad, F., Chen, ZG. *et al.* A second wave of topological phenomena in photonics and acoustics. *Nature* 618, 687–697 (2023).
- [4] Xue, H., Yang, Y. & Zhang, B. Topological acoustics. *Nat Rev Mater* 7, 974–990 (2022).
- [5] Shah, T., Brendel, C., Peano, V., & Marquardt, F. (2024). Colloquium : Topologically protected transport in engineered mechanical systems. *Reviews of Modern Physics*, 96(2).
- [6] Mousavi, S. H., Khanikaev, A. B., & Wang, Z. (2015). Topologically protected elastic waves in phononic metamaterials. *Nature Communications*, 6(1).
- [7] He, C., Ni, X., Ge, H., Sun, X., Chen, Y., Lu, M., Liu, X., & Chen, Y. (2016). Acoustic topological insulator and robust one-way sound transport. *Nature Physics*, 12(12), 1124–1129.
- [8] Brendel, C., Peano, V., Painter, O. J., & Marquardt, F. (2017). Pseudomagnetic fields for sound at the nanoscale. *Proceedings of the National Academy of Sciences*, 114(17).
- [9] Yu, S., He, C., Wang, Z., Liu, F., Sun, X., Li, Z., Lu, H., Lu, M., Liu, X., & Chen, Y. (2018). Elastic pseudospin transport for integratable topological phononic circuits. *Nature Communications*, 9(1).
- [10] Brendel, C., Peano, V., Painter, O., & Marquardt, F. (2018). Snowflake phononic topological insulator at the nanoscale. *Physical Review B*, 97(2).
- [11] Miniaci, M., Pal, R. K., Morvan, B., & Ruzzene, M. (2018). Experimental observation of topologically protected helical edge modes in patterned elastic plates. *Physical Review X*, 8(3).
- [12] Cha, J., Kim, K. W., & Daraio, C. (2018). Experimental realization of on-chip topological nanoelectromechanical metamaterials. *Nature*, 564(7735), 229–233.
- [13] Yan, M., Lu, J., Li, F., Deng, W., Huang, X., Ma, J., & Liu, Z. (2018). On-chip valley topological materials for elastic wave manipulation. *Nature Materials*, 17(11), 993–998.
- [14] Zhang, Z., Yu, S., Ge, H., Wang, J., Wang, H., Liu, K., Wu, T., He, C., Lu, M., & Chen, Y. (2021). Topological surface acoustic waves. *Physical Review Applied*, 16(4).
- [15] Zhang, Q., Lee, D., Zheng, L., Ma, X., Meyer, S. I., He, L., Ye, H., Gong, Z., Zhen, B., Lai, K., & Johnson, A. T. C. (2022). Gigahertz topological valley Hall effect in nanoelectromechanical phononic crystals. *Nature Electronics*, 5(3), 157–163.
- [16] Wang, J., Zhang, Z., Yu, S., Ge, H., Liu, K., Wu, T., Sun, X., Liu, L., Chen, H., He, C., Lu, M., & Chen, Y. (2022). Extended topological valley-locked surface acoustic waves. *Nature Communications*, 13(1).
- [17] Yan, M., Deng, W., Huang, X., Wu, Y., Yang, Y., Lu, J., Li, F., & Liu, Z. (2021). Pseudomagnetic fields enabled manipulation of On-Chip elastic waves. *Physical Review Letters*, 127(13).
- [18] Xu, X., Liu, Y., & Wu, T. (2024). On-chip topological phononic crystal acoustic waveguide based on lithium niobate thin films. *Applied Physics Letters*, 124(16).
- [19] Zhou, Y., Zhang, N., Bisharat, D. J., Davis, R. J., Zhang, Z., Friend, J., Bandaru, P. R., & Sievenpiper, D. F. (2023). On-Chip Unidirectional Waveguiding for Surface Acoustic Waves along a Defect Line in a

Triangular Lattice. *Physical Review Applied*, 19(2).

- [20] Delsing, P., Cleland, A. N., Schuetz, M. J. A., Knörzer, J., Giedke, G., Cirac, J. I., Srinivasan, K., Wu, M., Balram, K. C., Bäuerle, C., Meunier, T., Ford, C. J. B., Santos, P. V., Cerda-Méndez, E., Wang, H., Krenner, H. J., Nysten, E. D. S., Weiß, M., Nash, G. R., . . . Westerhausen, C. (2019). The 2019 surface acoustic waves roadmap. *Journal of Physics D Applied Physics*, 52(35), 353001.
- [21] Gong, S., Lu, R., Yang, Y., Gao, L., & Hassanien, A. E. (2021). Microwave Acoustic Devices: Recent advances and Outlook. *IEEE Journal of Microwaves*, 1(2), 601–609.
- [22] Huang, Y., Das, P. K., & Bhethanabotla, V. R. (2021). Surface acoustic waves in biosensing applications. *Sensors and Actuators Reports*, 3, 100041.
- [23] Makkonen, T., Plessky, V. P., Steichen, W., Chamaly, S., Poirel, C., Solal, M., & Salomaa, M. M. (2003). Fundamental mode 5 GHz surface-acoustic-wave filters using optical lithography. *Applied Physics Letters*, 83(17), 3596–3598.
- [24] Wang, M., Ma, Q., Liu, S., Zhang, R., Zhang, L., Ke, M., Liu, Z., & Chan, C. T. (2022). Observation of boundary induced chiral anomaly bulk states and their transport properties. *Nature Communications*, 13(1).
- [25] Xia, H., & Xiao, M. (2023). Reversal of the chiral anomaly bulk states with periodically staggered potential. *Physical Review B*, 107(3).
- [26] Zhang, Z., Lu, M., & Chen, Y. (2024). Observation of Free-Boundary-Induced chiral anomaly bulk states in elastic twisted kagome metamaterials. *Physical Review Letters*, 132(8).
- [27] Xia, B., Zhang, J., Jiang, Z., & Liu, J. (2024). Robust boundary-induced bulk propagations in elastic waveguides with nonplanar surfaces. *Science China Physics Mechanics and Astronomy*, 67(4).
- [28] Shen, S., Shang, C., Li, Y., & Zhang, Y. (2024b). Chiral Bulk Solitons in Photonic Graphene with Decorated Boundaries. *Laser & Photonics Review*, 19(3).
- [29] Lu, R., Yang, Y., Link, S., & Gong, S. (2020). A1 Resonators in 128° Y-cut Lithium Niobate with Electromechanical Coupling of 46.4%. *Journal of Microelectromechanical Systems*, 29(3), 313–319.